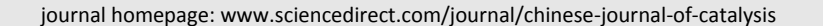


available at www.sciencedirect.com







Article

Constrained Al sites in FER-type zeolites (



Weifeng Chu ^{a,†}, Xiaona Liu ^{b,d,†}, Zhiqiang Yang ^c, Hiroya Nakata ^e, Xingzhi Tan ^c, Xuebin Liu ^c, Longya Xu ^a, Peng Guo ^{b,‡}, Xiujie Li ^{a,#}, Xiangxue Zhu ^{a,*}

- ^a State Key Laboratory of Catalysis, Dalian Institute of Chemical Physics, Chinese Academy of Sciences, Dalian 116023, Liaoning, China
- b National Engineering Laboratory for Methanol to Olefins, State Energy Low Carbon Catalysis and Engineering R&D Center, Dalian National Laboratory for Clean Energy, Dalian Institute of Chemical Physics, Chinese Academy of Sciences, Dalian 116023, Liaoning, China
- ^c Energy Innovation Laboratory, BP (China) Dalian Office, Dalian 116023, Liaoning, China
- d University of Chinese Academy of Sciences, Beijing 100049, China
- e Research Institute for Advanced Materials and Devices, Kyocera Corporation, Kyoto 619-0237, Japan

ARTICLE INFO

Article history: Received 7 April 2021 Accepted 28 May 2021 Available online 20 August 2021

Keywords:
FER-type zeolite
Aluminum siting
Structural characterization
Brönsted acid site
DME carbonylation

ABSTRACT

Crystallographic sites of Brönsted acids (Si-OH-Al) in zeolites, which are closely associated with the Al sites, play a significant and unique role in the catalytic application, especially when they are distributed in open channel systems or confined in cavities with small pore openings. In this article, we unraveled constrained Al crystallographic sites in **FER**-type zeolites containing the distinct local environments (10-ring channels and ferrierite cavities) by Rietveld refinement against the powder X-ray diffraction data. Final refinement demonstrates that regardless of the types of structure-directing agents and synthetic medium utilized, T1 and/or T3 are Al-rich positions, which are further confirmed by theoretical calculations. This new finding of constrained Al sites in the **FER**-type zeolite can well explain its limited catalytic activity in the DME carbonylation reaction.

© 2021, Dalian Institute of Chemical Physics, Chinese Academy of Sciences.

Published by Elsevier B.V. All rights reserved.

1. Introduction

Zeolites are microporous crystalline material with well-defined channels or cavities, which consists of core-sharing TO_4 (T = Si, Al, etc.). They are widely utilized in the petrochemical industry, fine chemical synthesis, modern coal chemical industry, etc. [1,2]. Among these applications, the distinctive shape selective catalysis is particularly noteworthy. The low-temperature dimethyl ether (DME) carbonylation

reaction [3–5] over zeolites discovered by Iglesia and co-workers [6] is a typical one used to produce methyl acetate (MA). Furthermore, this process could replace the environmentally unfriendly process of traditional methanol carbonylation using Rh or Ir organometallic complexes as catalysts and iodide compounds as promoters [7,8]. **FER-** and **MOR-**type zeolites have proved to be efficient catalysts for this process [3,4,9]. The **MOR-**type zeolite displays a high activity but a short lifetime. In order to extend its catalytic stability, pyridine

This work was supported by the National Natural Science Foundation of China (21972136, 22008229, 21773233, 21991091, U20A20120), CAS Pioneer Hundred Talents Program (Y706071202), Dalian National Laboratory for Clean Energy Cooperation Fund, Chinese Academy of Sciences (DNL201908), Liaoning Revitalization Talents Program (XLYC1908010, XLYC1901006), BP Energy Innovation Laboratory, and Scholarship from STOE.

 $DOI: 10.1016/S1872-2067(21)63884-6 \mid http://www.sciencedirect.com/journal/chinese-journal-of-catalysis \mid Chin.\ J.\ Catal.,\ Vol.\ 42,\ No.\ 11,\ November\ 2021(21)63884-6 \mid http://www.sciencedirect.com/journal/chinese-journal-of-catalysis \mid Chin.\ J.\ Catal.,\ Vol.\ 42,\ No.\ 11,\ November\ 2021(21)63884-6 \mid http://www.sciencedirect.com/journal/chinese-journal-of-catalysis \mid Chin.\ J.\ Catal.,\ Vol.\ 42,\ No.\ 11,\ November\ 2021(21)63884-6 \mid http://www.sciencedirect.com/journal/chinese-journal-of-catalysis \mid Chin.\ J.\ Catal.,\ Vol.\ 42,\ No.\ 11,\ November\ 2021(21)63884-6 \mid http://www.sciencedirect.com/journal/chinese-journal-of-catalysis \mid Chin.\ J.\ Catal.,\ Vol.\ 42,\ No.\ 11,\ November\ 2021(21)63884-6 \mid http://www.sciencedirect.com/journal/chinese-journal-of-catalysis |\ Chin.\ J.\ Catal.,\ Vol.\ 42,\ No.\ 11,\ November\ 2021(21)63884-6 \mid http://www.sciencedirect.com/journal/chinese-journal-of-catalysis |\ Chin.\ D.\ Catal.,\ Vol.\ 42,\ No.\ 11,\ November\ 2021(21)63884-6 \mid http://www.sciencedirect.com/journal/chinese-journal-of-catalysis |\ Chin.\ D.\ Catal.,\ Vol.\ 42,\ No.\ 11,\ November\ 2021(21)63884-6 \mid http://www.sciencedirect.com/journal/chinese-journal-of-catalysis |\ Chin.\ D.\ Catal.,\ Vol.\ 42,\ No.\ 11,\ November\ 2021(21)63884-6 \mid http://www.sciencedirect.com/journal/chinese-journal-of-catalysis |\ Chin.\ D.\ Catal.,\ Vol.\ 42,\ No.\ 42,\$

^{*} Corresponding author. Tel/Fax: +86-411-84379279; E-mail: zhuxx@dicp.ac.cn

[#] Corresponding author. Tel/Fax: +86-411-84379279; E-mail: xiujieli@dicp.ac.cn

^{\$} Corresponding author. Tel: +86-411-84379149; Fax: +86-411-84379289; E-mail: pguo@dicp.ac.cn

[†] These authors contributed equally.

(Py) molecules are usually applied to block Brönsted acid sites (BASs) in the 12-ring channels [4,5]. In contrast, the **FER**-type zeolite shows good catalytic stability without further modification, but relatively low activity [3,10,11].

From the crystallographic point of view, it is of significance to note that FER- and MOR-type zeolites possess the distinct local environments such as open channel systems and cavities/side pockets with small pore openings (delimited by 8 T atoms). As shown in Fig. 1(a), the FER framework has 10-ring channel systems along the c-axis and ferrierite cavities with 8-ring pore openings along the b-axis. T1, T2, and T3 in the **FER** framework can be accessed through 10-ring channels or ferrierite cavities, while T4 can only be contacted through ferrierite cavities (note: labels of T atoms have been unified according to the FER framework in the international zeolite association (IZA)). MOR framework has 12-ring channels along the c-axis and side pockets. T1, T2, and T4 belong to either 12-ring channels or side pockets, while T3 is affiliated to side pockets solely (Fig. S1). From the synthetic point of view, the location of Al atoms in certain zeolite frameworks can be tunable and governed by some synthetic parameters such as alkali metal ions [12,13] and organic structure-directing agents (OSDAs) [11,14,15]. It was found that the active sites in DME carbonylation were located in side pockets of MOR or in the ferrierite cavities of FER [9]. Then Al atoms confined in cavities or side pockets will definitely make distinct impacts on DME carbonylation reaction. For the FER-type zeolite catalyst, since it can catalyze the unique DME carbonylation reaction without any further modifications, researchers have tried to selectively allocate more Al atoms in ferrierite cavities by controlled synthesis using different OSDAs, synthetic mediums, and synthetic methodologies [10,11]. However, improvements of their catalytic performance are still limited. Moreover, precisely identifying and controlling Al atoms on different T sites of FER-type

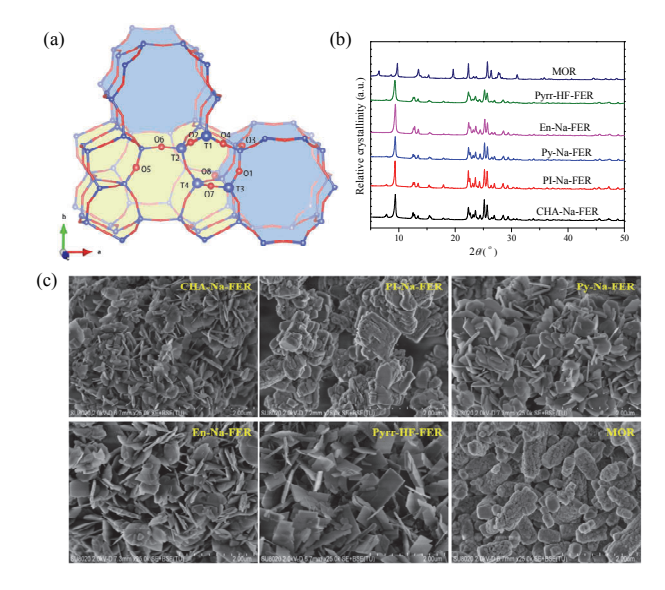


Fig. 1. (a) **FER**-type zeolite framework. For better understanding, the 10-ring channels and ferrierite cavities are highlighted in blue and yellow, respectively. Atom color: blue: T, red: O. (b) PXRD patterns of **FER**- and **MOR**-type zeolites; (c) SEM images of sample CHA-Na-FER, PI-Na-FER, Py-Na-FER, En-Na-FER, Pyrr-HF-FER, and **MOR**-type zeolite.

zeolite are also of great challenge.

Conventional approaches such as temperature-programmed desorption of ammonia (NH3-TPD), pyridine (Py)-adsorbed Fourier transform infrared spectroscopy (FT-IR), and ¹H MAS NMR spectra can only provide acid densities, acid strength, rough distribution of BASs, rather than their atomic sites. The calculation of substitution energies of Al atoms based on the theoretical FER-type framework can provide the atomic coordinates of Al sites, however, this process neglects the influences of synthetic conditions, such as OSDAs, the silicon source, aging time, etc. [16]. Compared with aforementioned methods, Rietveld refinement against diffraction data is a powerful tool to explore the Al sites at the atomic level in the FER-type zeolite experimentally [17-19]. Using Rietveld refinement against powder X-ray diffraction (PXRD) data of as-made samples, Pinar et al. have demonstrated the success of tuning Al-rich positions from T1 to T3 sites in the FER-type zeolite (Si/Al = 15.4 and 16.1) through judiciously selecting OSDAs in the fluoride medium [17]. Our group has also investigated the Al distribution in FER-type zeolite (Si/Al = 26.1) synthesized in a system containing Py and Na+ and found that the T1 site is an Al-rich position in this sample [18].

Herein, we deliberately synthesized a series of **FER**-type zeolites with cyclic and linear OSDAs in the hydroxide and fluoride medium, respectively. We combined Rietveld refinement with simulated annealing algorithms to investigate Al sites in the as-made and probe molecules (PMs) Py adsorbed **FER**-type zeolite samples at the atomic level. Furthermore, DME carbonylation was chosen as a probe reaction to evaluate the catalytic performance of obtained **FER** samples. We expect to clarify the relationship between Al siting in **FER**-type zeolite and its limited catalytic activity in DME carbonylation reaction.

2. Experimental

2.1. Sample preparation

2.1.1. Synthesis of FER-type zeolites with OSDAs and Na+

The general synthesis procedure was carried out as follows: silica sol (30.6 wt% SiO₂, Qingdao Haiyang Chemical Co., Ltd.) was added to a solution containing sodium aluminate (16.8 wt% Al₂O₃, 24.2 wt% Na₂O, home-made) and water. Then this mixture was transferred into a 100 mL stainless-steel autoclave. After that, sodium hydroxide solution (0.1 g/mL, Sinopharm Chemical Reagent Co., Ltd.), and cyclohexylamine (CHA) were consecutively added into this autoclave under stirring. Then the initial gel mixture with compositions of 1.73Na₂O: 0.66Al₂O₃: 20SiO₂: 3.2CHA: 280H₂O, was obtained. This mixture was first kept stirring at 25 °C for 0.5 h and then heated at 160 °C for 48 h (60 rpm). After crystallization, the synthetic process was quenched with tap water. The product was obtained by centrifugation several times before drying at 120 °C overnight. The well-crystallized sample was assigned as m-n-FER, where m and n represented OSDA and Na, respectively. Pure zeolite samples were also synthesized with piperidine (PI)/Na+, pyridine (Py)/Na+, ethylenediamine (En)/Na+,

and the detailed initial gel compositions and synthetic conditions were summarized in Table S1.

2.1.2. Synthesis of **FER**-type zeolite with pyrrolidine (Pyrr) and HF

FER-type zeolites were synthesized with Pyrr and HF according to the reported reference with slightly modification [17]. Typically, tetraethyl orthosilicate (TEOS, Sinopharm Chemical Reagent Co., Ltd.) and aluminum isopropoxide (Sinopharm Chemical Reagent Co., Ltd.) were added to the solution of water and a portion of Pyrr, and then the silicon and aluminum sources were fully hydrolyzed at 80 °C. After that, the rest Pyrr was added and evaporated water was supplied. The HF acid was carefully introduced into the solution. Finally, the initial gel mixture with compositions of 0.66Al₂O₃: 20SiO₂: 11.4Pyrr: 320H2O: 10.2HF, was obtained. After stirring at 25 °C for 0.5 h, the mixture was crystallized at 170 °C for 120 h with stirring (60 rpm). Then the crystallization process was quenched with tap water. The product was obtained by centrifugation several times before drying at 120 °C overnight. The well-crystallized sample was assigned as Pyrr-HF-FER.

2.1.3. Synthesis of **MOR**-type zeolite with tetraethylammonium hydroxide (TEAOH) and Na⁺

MOR zeolite was synthesized with TEAOH and Na⁺ according to the reported reference with a slight modification [4]. Typically, sodium aluminate (55.1 wt% Al₂O₃, 44.9 wt% Na₂O, Sinopharm Chemical Reagent Co., Ltd.), deionized water, silica sol (30.6 wt% SiO₂), sodium hydroxide solution (0.1 g/mL), TEAOH (35% in the water, SACHEM), and **MOR** seeds (2.0 wt% respect to the mass of SiO₂ and Al₂O₃) were consecutively added into a stainless-steel autoclave under stirring. Then the initial gel mixture with compositions of 1.93Na₂O: 0.60Al₂O₃: 20SiO₂: 4TEAOH: 320H₂O, was obtained. After stirring at 25 °C for 0.5 h, the mixture was heated under rotation (40 rpm) at 175 °C for 48 h. After crystallization, the synthetic process was quenched with tap water. The product was obtained by centrifugation several times before drying at 120 °C overnight. The well-crystallized sample was denoted as MOR.

2.1.4. Preparation of proton-form samples

The **FER**-type zeolite samples obtained with OSDA and Natwere calcined at 500 °C for 6 h to remove the OSDA. Then 1.0 mol/L NH₄NO₃ solution was used to exchange with the calcined Na-form samples. After exchanging at 80 °C for 2 h (three times) and calcining at 500 °C for 3 h, the proton-form zeolites were obtained. The obtained proton-form samples were pressed into tablets, crushed, and sieved into 20–40 mesh particles. The preparation process of proton-form **MOR**-type zeolite was the same as proton-form **FER**-type zeolite samples.

The proton-form Pyrr-HF-FER was obtained by directly calcining the as-synthesized sample at 500 $^{\circ}\text{C}$ for 6 h.

2.2. Characterization

PXRD data for the phase identification were collected on a PANalytical Empyrean-100 diffractometer using Cu K_{α} radiation operating at 40 kV and 40 mA. The high-resolution STOE STADI P ESSENTIAL diffractometer (Cu $K_{\alpha 1}$, λ = 1.5406 Å) was used to record PXRD data used for Rietveld refinement. The experiments were performed in the Debye-Scherr mode. The diameter of the capillary is 0.2 mm. Before data collection, samples were dehydrated at 200 °C for 12 h. For the identification of nitrogen in the Py, we adopted the methodology reported by Pinar *et al.* [17]. The distances between each C/N atom in the probe molecule pyridine and 0 atoms in **FER** framework were measured. If distances are close to 3 Å and angles between 0, H, and C/N atoms are close to 180°, we identify the atom in pyridine is N and the protonated pyridine form the hydrogen bonding with the **FER** framework.

Chemical compositions of **FER**-type and **MOR**-type zeolite samples were analyzed using a PANalytical Axios advanced X-ray fluorescence spectrometer.

Morphologies and particle size of samples were observed by Hitachi SU8020 scanning electron microscope.

 N_2 adsorption-desorption experiments were performed at $-196\ ^\circ C$ on a Micromeritics ASAP-2020 HD88 instrument. Prior to the data collection, all the samples were degassed at 350 $^\circ C$ for 5 h.

Thermogravimetric analysis (TGA) was carried out with Pyris Diamond TG/DTA analyzer or TA Q-600 analyzer. As-made samples were heated in the temperature range from 35 °C to 850 °C at a ramp rate of 10 °C/min under air with a flow rate of 60 mL/min. Py-adsorbed samples were measured at a rate of 10 °C/min from room temperature to 900 °C under air with a flow rate of 100 mL/min.

All solid-state MAS NMR experiments were carried out on a Bruker Avance III 400 MHz spectrometer. ^{13}C CP/MAS NMR and ^{27}Al MAS NMR spectra were acquired at 100.6 and 104.3 MHz using a 4 mm MAS NMR probe. ^{27}Al MAS NMR spectra were accumulated for 512 scans with a spinning rate of 8 kHz, $\pi/12$ flip angle, and 1 s recycle delay. Chemical shifts were referenced to 1 M Al(NO₃)₃ aqueous solution. ^{13}C CP/MAS NMR experiments were accumulated for 3000 scans with a spinning rate of 12 kHz, CP contact time of 500 μs and a recycle delay of 2 s.

NH₃-TPD experiments were measured in a quartz micro-reactor (i.d. 4 mm) which was connected to an online Shimadzu GC-8A gas chromatograph equipped with a thermal conductivity detector (TCD). The integral area of TCD response was calibrated by injecting NH₃ of known amounts. In a typical experiment, the proton form sample (140 mg) was pretreated at 600 °C for 0.5 h under continuous He flows (25 mL/min). Then the samples were cooled down to 150 °C and saturated with NH₃. After that, He flow was used to purge the physical adsorption NH₃ and that in the gas phase. Finally, the samples were heated from 150 to 600 °C at a heating rate of 19.6 °C/min.

In adsorption of Py molecules, the proton-form samples were put into a quartz tubular reactor. Prior to the adsorption process, the samples were heated to 500 or 400 $^{\circ}$ C and maintained at this temperature for 1 h in the presence of N₂. After

that, the samples were cool down to 300 °C naturally and started to adsorb Py molecules. Py was fed by passing the N_2 through a saturator containing Py at room temperature. After adsorbing Py for 60 h, the samples were maintained at 300 °C for another 1 h under N_2 flow. Finally, the samples were cool down to room temperature and sealed for further measurements.

2.3. Dimethyl ether (DME) carbonylation

DME carbonylation reaction was carried out in a stainless-steel fixed bed reactor with an inner diameter of 9.5 mm at $160~^{\circ}$ C and 3.0 MPa. Typically, 0.5 g of catalyst (20–40 mesh) was put into the center of the reactor and pretreated in continuous N₂ flow at $400~^{\circ}$ C for 2 h. After that, the temperature was cooled down to $160~^{\circ}$ C, and then the gas mixture of DME, CO, and N₂ (internal standard) with a molar ratio of 4/91/5was introduced into the reactor. The gas hourly space velocity (GHSV) of total gas flow was $3000~h^{-1}$. The reaction effluents were kept in the vapor phase and analyzed by an online Agilent 3000A~micro~gas~chromatograph. The synthesis rate of MA was calculated according to the following equation:

MA synthesis rate $(mol/(mol H+\cdot h)) = (MA molar flowrate (mol/h))/(catalyst amount (g) × acid amount (mol H+/g))$

2.4. Theoretical calculation

The interaction energies were evaluated with the density functional theory (DFT) program SIESTA [20–22]. The simulations were performed with the Perdew-Burke-Ernzerhof (PBE) function [23,24], and norm-conserving pseudopotentials were used [25]. The energy cutoff was 300.0 Ry. Grimme's correction was employed to evaluate the dispersion interactions [26].

To evaluate the stable Al site, the Si site was replaced with Al and then the hydrogen atom was inserted to the nearest oxygen atom to keep the neutrality condition. The geometry optimizations of Al substitution were performed with four steps: First, the geometry of only the inserted Hydrogen and covalently bonded oxygen atom was optimized (1st sphere from H). Then, the Al and Si next to the oxygen atom were added to the geometry optimized region (2nd sphere). Likewise, the geometry optimizations were performed for the 3rd

and 4th sphere from the inserted hydrogen atom. This step by step geometry optimization keeps the optimized geometry consistent.

3. Results and discussion

3.1. Conventional characterizations of FER-type zeolites

A series of as-made FER-type zeolites synthesized by PI, CHA, Py, and Pyrr as OSDAs are denoted as m-n-FER, where m and n indicate OSDA and Na/HF, respectively. The details of gel compositions and synthetic conditions are listed in Table S1. As shown in Figs. 1(b) and (c), these four as-made FER-type samples are well-crystallized with traditional plate-like morphologies. According to X-ray fluorescence spectroscopy (XRF) results (Table 1), the Si/Al molar ratios (SAR) of these samples range from 12.6 to 13.2. Moreover, the molar ratios of sodium to aluminum (Na/Al) for PI-Na-FER, CHA-Na-FER, and Py-Na-FER are 0.11, 0.36, and 0.80, respectively. The number of OSDAs, H₂O, and PMs Py could be deduced from thermogravimetric analysis (TGA) and summarized in Table S2. Considering the charge balance of FER-type zeolite, all these OSDAs are partially protonated and the protonated ratios are different. Their textural properties and acid densities are summarized in Table 1, which are calculated from N₂ adsorption and NH₃-TPD experiments (Fig. S2 and Fig. 2(a)). The surface area and micropore volume of these four samples are approximately to 390 m²/g and 0.130 cm³/g, respectively. The acid amounts of the aforementioned samples range from 1.03 to 1.11 mmol/g. This indicates that these as-made samples directed by different OSDAs have similar physical and chemical properties. 13C CP/MAS NMR (Fig. S3) spectra of as-made samples indicate that the occluded OSDAs are intact. ²⁷Al MAS NMR spectra (Fig. 2(b)) of the proton-form samples show just one peak centered at around 55 ppm, indicating that all the Al species are incorporated into the framework as tetrahedral geometries.

Since proton-form zeolites are considered as crystalline porous solid acids, it can interact with basic PMs Py, generating classical hydrogen bonding. Thus, we also investigated the acid properties of **FER**-type zeolites with Py adsorption experiments. As shown in Table 1, when the Py adsorption reached equilibrium at 300 °C, there are 2.2, 2.0, 2.0, and 1.8 Py identi-

Table 1XRF results, textural properties, and acid amounts of **FER**-type and **MOR**-type zeolites.

					-	•				
Sample	SAR a	Na/Al a -	Surface area (m ² /g)			Pore volun	Pore volume (cm ³ /g)		Number of	Percentage of
			$S_{ m BET}$	$S_{ m micro}$	$S_{ m ext}^{\ m b}$	$V_{ m micro}$ b	$V_{ m meso}$	(mmol/g)	Py d	T2 and/or T4 e
PI-Na-FER	12.6	0.11	384	338	46	0.130	0.094	1.10	2.2	18%
CHA-Na-FER	13.2	0.36	397	340	57	0.131	0.218	1.03	2.0	20%
Py-Na-FER	13.2	0.80	390	344	46	0.131	0.114	1.03	2.0	20%
En-Na-FER	10.9	0.03	395	333	62	0.128	0.238	1.22	2.3	20%
Pyrr-HF-FER	13.0	_	392	334	58	0.128	0.163	1.11	1.8	30%
MOR	12.4	0.72	566	505	61	0.193	0.088	0.96	_	_

 a Contents of Si, Al, and Na are determined by XRF. b $S_{\rm ext}$ and $V_{\rm micro}$ are determined by t-plot method. c Acid amount was measured by NH₃-TPD. d The number of Py per unit cell when Py adsorption (performed at 300 o C) reached equilibrium. Based on the following Rietveld refinement results, the number of Py per unit cell is related to the number of Al atoms in T1 and/or T3 sites within one-unit cell. e The percentage of T2 and/or T4 is calculated from Py-adsorption experiments, TG measurements, and Rietveld refinements, which can be expressed as the following formula: percentage of T2 and/or T4 = (the number of Al atoms per unit cell – the number of Py per unit cell)/the number of Al atoms per unit cell × 100%.

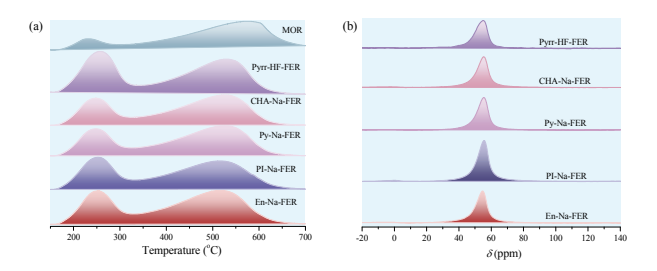


Fig. 2. (a) NH₃-TPD profiles of proton-form **FER**- and **MOR**-type zeolites (b) ²⁷Al MAS NMR spectra of proton-form CHA-Na-FER, PI-Na-FER, Py-Na-FER, En-Na-FER, and Pyrr-HF-FER.

fied in the unit cell of PI-Na-FER, CHA-Na-FER, Py-Na-FER, and Pyrr-HF-FER, respectively. However, such conventional characterization approaches can provide nothing about the distributions of BASs at the atomic level. Fortunately, these pure samples with good crystallinities enable us to investigate BASs by refining both as-made and Py-adsorbed zeolite structures against PXRD data through Rietveld refinement.

3.2. Rietveld refinement results of CHA-Na-FER and CHA-Na-FER-Py-60h samples

Among this series of samples of interest, we selected CHA-Na-FER as an example for the detailed description of Rietveld refinement process. The idealized FER framework (including the unit cell parameters, space group, and atomic coordinates) in IZA is adopted as the initial structure model [27]. It has 4 T atoms and 8 O atoms in the asymmetric unit with the space group Immm (NO. 71). Since the high angle data is not affected significantly by the guest species in the 10-ring channels and ferrierite cavities, we can obtain an appropriate scale factor between the experimental (blue line) and simulated (red line) data based on data from 60° to 120° in 2θ . The electron densities within the 10-ring channels and ferrierite cavities were obtained by applying this scale factor to the whole pattern. As shown in Fig. S4, there are clouds of electron densities and electron density dots in ferrierite cavities and 10-ring channels, respectively. It indicates that CHAs are embedded in ferrierite cavities only and Na+ locates in the 10-ring channels. The simulated annealing algorithm was employed to determine the initial locations of CHA. This algorithm was originally developed as a direct (real)-space method for the structure determination. For example, a 1D 12-ring aluminophosphate molecular sieve UiO-6 (OSI) and a 1D 8-ring aluminosilicate ERS-7 (ESV) were solved by simulated annealing algorithm [28,29]. Recently, it has been extended to investigate host-guest interactions in the crystalline porous materials [30,31]. After determining the initial positions of OSDAs, such parameters as atomic coordinates (framework atoms and guest species), unit cell dimensions, peak shape functions, background, etc. are further refined. All the structural results are displayed in Figs. 3(a)-3(c) and Tables S3 and S4. The final refinement reveals that Na+ is distributed in the 10-ring channel system and the distances between Na+ and two O1 atoms are shorter than other framework oxygens (as shown in Fig.

3(b) and Table S4). This indicates that T3 is an Al-rich position. According to XRF, Na $^+$ balances 36% of negative charges from the zeolite framework of CHA-Na-FER, while the rest are compensated by protonated CHAs. It also indicates that most CHA molecules (70%) are protonated. It is interesting to note that CHAs are identified in ferrierite cavities solely and the NH $_2$ /NH $_3$ $^+$ groups point to the 8-ring pore opening of ferrierite cavities. The shortest distance of O3 (bridging two T1 sites) and N atoms of CHAs is 2.76 Å (Fig. 3(c) and Table S4), indicating the T1 site is another Al-rich position.

In order to further confirm our hypothesis that T1 and T3 sites are Al-rich positions, the Py-adsorbed sample denoted as CHA-Na-FER-Py-60h was prepared and then refined against PXRD data as well (Figs. 3(d)–3(f), Fig. S5, and Tables S3, S4). It is expected that the protonated PMs Py will interact with framework oxygens associated with T1 (O1, O2, O3, and O4) and T3 sites (O1, O7, and O8), rather than other framework oxygens. The final refinement demonstrates that PMs Py in this sample are identified in both 10-ring channels and ferrierite cavities. After checking the distance between the protonated PMs Py and O atoms in **FER** framework (Fig. S6), we found PMs Py in the 10-ring channel have the classical hydrogen bonding with O2 ([C,N]-H2...O2: 3.24 Å) (Fig. 3(d) and Table S4). It is worth noting that a portion of PMs Py can be identified in the ferrierite cavities (Figs. 3(e) and 3(f)). The shortest distance

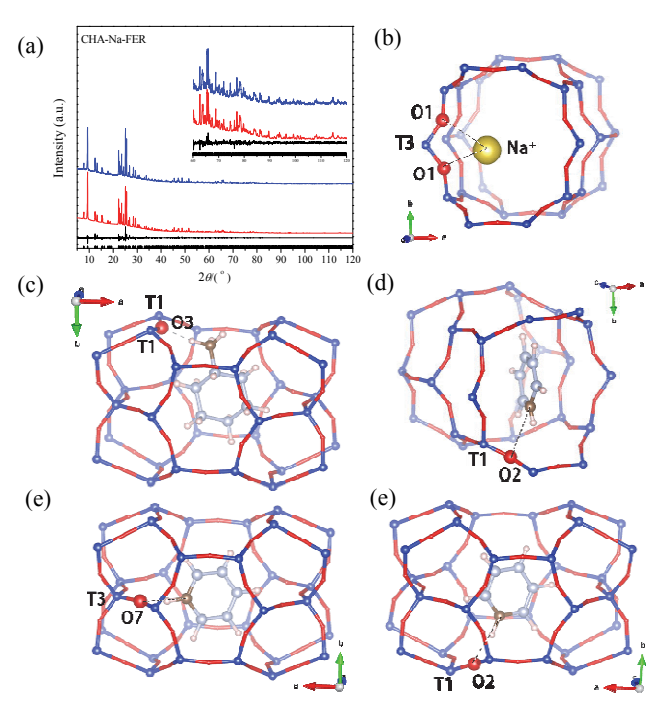


Fig. 3. Rietveld refinement results of CHA-Na-FER and CHA-Na-FER-Py-60h samples. (a) Final Rietveld refinement plot of CHA-Na-FER. The observed, calculated, and difference curves are in blue, red, and black, respectively. The vertical bars indicate the positions of Bragg peaks. The insert is enlarged high angle part. (b,c) Na⁺ and CHA locate in the 10-ring channels and ferrierite cavities of CHA-Na-FER, respectively. (d-f) For CHA-Na-FER-Py-60h sample, the protonated Py is occluded in the 10-ring channels and ferrierite cavities Atom color: blue: Si or Al, red: O, yellow: Na⁺, saddle brown: N, navy blue: C, misty rose: H.

between N atoms in Py and framework O (07) is 3.14 Å (Fig. 3(e) and Table S4). Compared with the distance of [C,N]-H11...07, the distance of [C,N]-H12...02 (3.27 Å) can also be considered in the scope of hydrogen bonding (Fig. 3(f) and Table S4). It means that the protonated PMs Py confined in the ferrierite cavities could probe BASs associated with T1 or T3 sites. Therefore, T1 and T3 sites are Al-rich positions revealed from Rietveld refinement of as-made CHA-Na-FER, which are further confirmed by the refinement of the Py-adsorbed sample.

3.3. Rietveld refinement results of Py-Na-FER and Py-Na-FER-Py-60h samples

We also select another sample Py-Na-FER templated by Na+ and Py as SDAs for further investigation. It is of interest to note that 80% of the negative charges from the zeolite framework are balanced by inorganic cations as demonstrated in Table 1. Its scenario is distinct from the CHA-Na-FER sample, in which most of negative charges are balanced by OSDAs, rather than inorganic cations. In order to explore the distribution of Na+ and Py, Rietveld refinement combined simulated annealing algorithm was also employed. The results showed that Py molecules (OSDAs) are in both 10-ring channels and ferrierite cavities, while Na ions can only be identified in the 10-ring channels (Figs. S7, S8, and Table S3, S4). Moreover, as illustrated in Fig. S7(a), Na ion is mainly balanced the negative charges from the substitution of Si by Al at T1 and T3 sites. Only a small portion (19%) of Py is protonated based on the unit cell composition as listed in Table S2. Hence, it is challenging for us to identify the locations of protonated Py. After adsorbing PMs Py at 300 °C of proton-form FER-type zeolite, the Py-Na-FER-Py-60h was prepared. Subsequently, we refined this sample again to probe the locations of PMs Py. It turned out that PMs Py are distributed in both 10-ring channels and ferrierite cavities, which interact with BASs associated with Al located in T1 and T3 (Figs. S9, S10 and Tables S3, S4). Therefore, Rietveld refinements on Py-Na-FER and Py-Na-FER-Py-60h samples further display that T1 and T3 are Al-rich positions.

3.4. Rietveld refinement results of other **FER**-type zeolites

We also investigated Al sites in **FER**-type zeolites templated by other OSDAs through utilizing the same method. For PI-Na-FER, the amount of Na ions is too low to be identified. We can only locate PI in the 10-ring channels and ferrierite cavities. The refinement results indicate that T1 and T3 are Al-rich positions (Figs. S11, S12 and Table S4). The Al-rich T sites in the Pyrr-HF-FER had been investigated through refining the as-made sample previously [17]. It turned out the T3 site is an Al-rich position. Subsequently, in order to further verify our results, PMs-adsorbed samples (PI-Na-FER-Py-60h and Pyrr-HF-FER-Py-60h) were refined against PXRD data, demonstrating that PMs Py are distributed in the 10-ring channels and ferrierite cavities as well (Figs. S13-S16). The shortest framework oxygen-guest (PMs Py) distances in Py-adsorbed samples are listed in Table S4. Combined with refinement results of

as-made and PMs-adsorbed samples, it can be concluded that T1 and/or T3 are Al-rich positions no matter what types of OSDAs and the synthetic medium were utilized. The PMs Py adsorbed in all the **FER**-type zeolites are related to BASs associated with T1 or/and T3. In this case, the percentage of T2 or/and T4 can be deduced as illustrated in Table 1. Moreover, we also calculate the substitution energies of Al at each T site, in which the proton locations are also considered. It was found that the substitution energies related to T1-02 (0.0894 eV), T1-03 (0.0000 eV), T3-07 (0.1939 eV), and T3-08 (0.1189 eV) sites were much lower than other sites (0.4150–0.7742 eV). Therefore, Al will be prone to locate T1 and T3 sites, which are in consistent with our experimental results (Table S5).

3.5. Theoretical calculations of interactions between protonated pyridines and zeolite framework

Based on the results unraveled from Rietveld refinements, there are two issues that are not easy to understand. Firstly, now that T3 sites are Al-rich positions, why do the PMs Py interact with 07/08 confined in the ferrierite cavities rather than O1 distributed in the open 10-ring channels? It is attributed to the fact that the 10-ring channel is elliptical ($5.4 \times 4.2 \text{ Å}$), which cannot accommodate the Py lying on the ac-plane. Therefore, after entering into the 10-ring channels, PMs Py are forced to pass through the 8-ring pore openings and enter ferrierite cavities to access BASs associated with T3 (Fig. 4(a)). Secondly, Rietveld refinement of PMs Py-adsorbed samples demonstrated that BASs associated with Al-rich T1 sites could be accessible by Py from 10-ring channel systems and ferrierite cavities (Figs. 3(d) and 3(f), Figs. S13(a) and S13(c))). Now there is an interesting question: given that BASs associated with Al-rich T1 sites can directly interact with PMs Py distributed in 10-ring channels (Fig. 3(d) and Fig. S13(a)), is it necessary for PMs Py to access those through entering ferrierite cavities (Fig. 3(f) and Fig. S13(c))? This phenomenon can be illustrated in the following way: it is obvious that one 10-ring channel can only accommodate one PM Py. If there are two Al atoms locating in T1 sites in the 10-rings simultaneously (Fig. 4(b)), one protonated PM Py in the 10-ring channel system can only interact with one of them. Therefore, it forces the PMs Py to enter ferri-

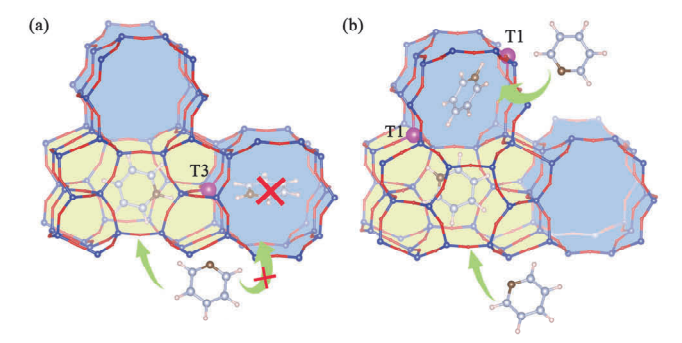


Fig. 4. Schematic illustration of interactions between Py and **FER**-type zeolites. (a) T3 site is Al-rich position. (b) There are two Al atoms locating in T1 sites. For better understanding, the 10-ring channels and ferrierite cavities are highlighted in blue and yellow, respectively. Atom color: blue: Si, purple: Al, red: O, saddle brown: N, navy blue: C, misty rose: H.

erite cavities to contact BASs associated with the other one (Fig. 4(b)). In order to further understand both interesting phenomena, we performed theoretical calculations on the interaction energies of Py located in the 10-ring channels or ferrierite cavities when Al atoms were distributed in the T1 or T3 sites. When T3 sites are Al-rich positions, protonated PMs Py in ferrierite cavities interacting with 07/08 show much lower interaction energies (-506.96 and -469.03 kJ/mol as shown in Fig. 5(a) and 5(b)). It is of importance to note that the interaction energy (-426.05 kJ/mol as shown in Fig. 5(c)) becomes much higher when protonated Py interacts with 01 (associated with T3 sites) in the 10-ring channels. It can well explain why the PMs Py need to pass through 8-ring pore openings, interacting with 07 or 08 confined in ferrierite cavities. When T1 sites are Al-rich positions, the initial structural models become complicated since 02 and 03 could be accessible by protonated PM through cavities and 10-ring channels (Figs. 5(d)-5(g)). Our calculation results indicate that protonated PMs Py located in the ferrierite cavities have lower interaction energies (-514.07 kJ/mol and -492.16 kJ/mol as shown in Figs. 5(d) and (e)) than the ones in the 10-ring channels (Figs. 5(f)-(h)). Therefore, it is reasonable that the protonated Py can interact with BASs associated with T1 in the ferrierite cavities. It is worth pointing out that the structural model displayed in Fig. 5(h) has a relative higher interaction energy (-418.31 kJ/mol), whose scenario is quite similar to the structural model depicted in Fig. 5(c). Both structural models have relatively high interaction energies and the hydrogen bonding angles deviate from the idealized one (180°) largely (Table S6). Such higher interaction energies result from the elliptical 10-ring opening, which is challenging to accommodate Py lying in the ac-plane. More importantly, both structural models are not observed in the experimental either. In other words, combined with our experimental Rietveld refinement results with theocratical calculations, PMs Py in the 10-ring channels interact with BAs associating with T1 sites solely, while PMs Py confined in the ferrierite cavities could contact BASs belonging to T1 and/or T3 sites.

3.6. DME carbonylation performance of **FER**- and **MOR**-type zeolites

The DME carbonylation reaction is chosen as a probe reaction to further evaluate the Al sites as it has been well accepted the carbonylation activity is closely related to the number of BASs in ferrierite cavities or side pockets in MOR-type zeolite [9]. Our previous work investigated the active centers catalyzing carbonylation of DME over FER-type zeolite through quantum-chemical method. We found T4-07 and T2-05 of FER-type zeolite are the active sites for DME carbonylation considering the reaction energies of forming surface methoxy group (SMG) and activation energies for the reactions of CO, H2O, CH3OH and DME with SMG [32]. In general, the ratio of BASs in side pockets were around 45%-55% for MOR-type zeolite [4,9], while that on T2/T4 of **FER**-type zeolite was only 18%–30% on basis of the Py adsorption, TG, and Rietveld refinement results in this work. On the premise of the similar contribution of BASs to the DME carbonylation reaction, the catalytic activity of FER-type zeolites should be below the half activity of the MOR-type zeolite. In Fig. 6, PI-Na-FER, Py-Na-FER, and CHA-Na-FER catalysts display the similar MA synthesis rate (~0.10 mol/(mol H+·h)), while Pyrr-HF-FER prepared in the fluoride medium exhibits higher synthesis rate (0.16 mol/(mol H+·h)) of MA, which might be attributed to relatively high BASs associated with T2/T4 sites as demonstrated in Table 1. However, its MA synthesis rate is just half of the one of MOR-type zeolite (0.40 mol/(mol H+·h)) as shown in Fig. 6. It was noteworthy that no deactivation phenomenon was observed over MOR-type zeolite in 50 h (Fig. S17). The above results are in good accordance with our hypothesis. Moreover, according to DME carbonylation catalytic results and Rietveld refinements, it turns out that tuning Al

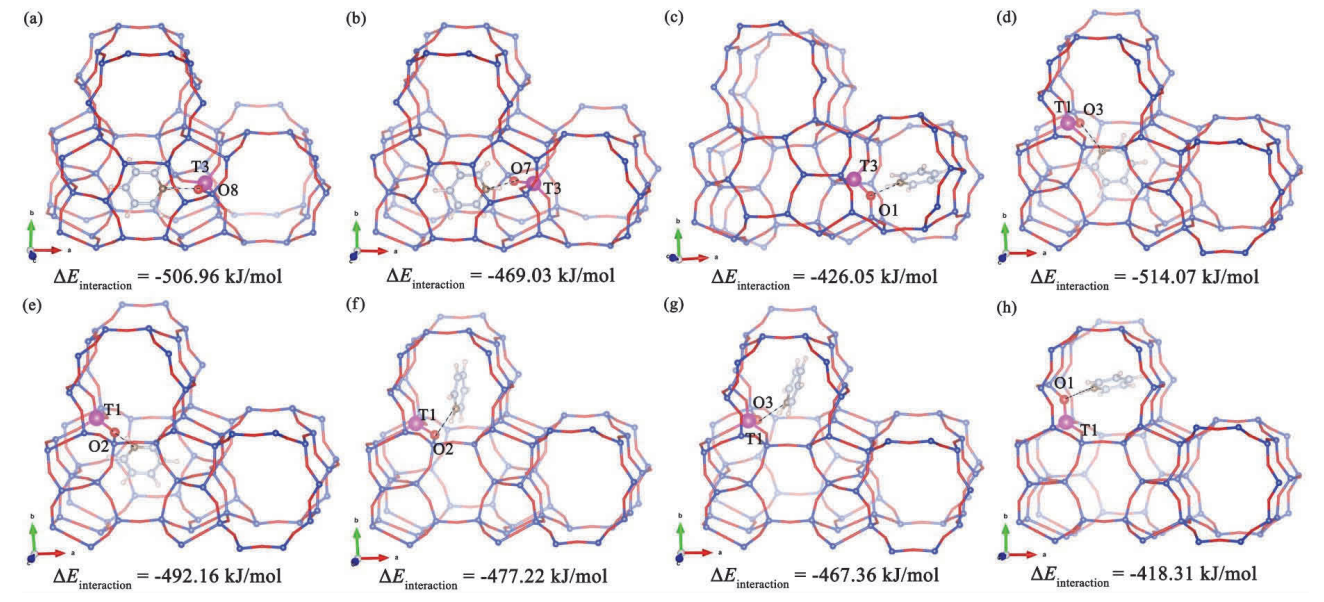


Fig. 5. Optimized structures and the calculated $\Delta E_{\text{interaction}}$ of Py locating in 10-ring channels and ferrierite cavities. (a–c) T3 sites are Al-rich positions; (d–h) T1 sites are Al-rich positions. Atom color: blue: Si, purple: Al, red: O, saddle brown: N, navy blue: C, misty rose: H.

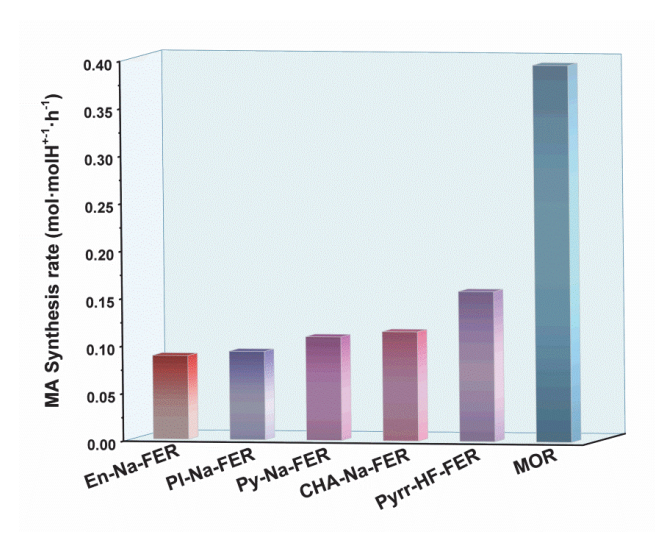


Fig. 6. MA synthesis rate per H $^+$ over **MOR-** and a variety of **FER-**type zeolites. Reaction conditions: 160 °C, 3.0 MPa, GHSV = 3000 h $^{-1}$, DME/CO/N₂ = 4/91/5, TOS = 50 h.

sites in **FER**-type zeolites is limited and most of the Al atoms are constrained on T1 and/or T3 sites no matter what types of SDAs or synthetic medium are utilized. This well explains the relatively low activity of **FER**-type zeolite in DME carbonylation reaction. In order to further confirm our new findings regarding the constrained Al sites in **FER**-type zeolite, another **FER**-type zeolite catalyst was prepared by the linear OSDA ethylenediamine (En) and inorganic cation Na⁺. It is worth noting that its SAR becomes much lower (3.0 Al atoms per unit cell). If Al atoms are not constrained at T1 and T3 sites, its DME carbonylation performance should be superior to the other four **FER**-type zeolites. However, its MA synthesis rate is similar to that of the other **FER**-type catalysts prepared with cyclic OSDAs in the hydroxide medium. Rietveld refinement combined simulated annealing algorithm are also applied to

as-made (En-Na-FER) and PMs Py-adsorbed (En-Na-FER-Py-60h) samples for probing the Al sites. Final results show that T1 and T3 are still Al-rich positions as illustrated in Figs. S18–S21, and Tables S3, S4.

4. Conclusions

In this work, five **FER** samples (denoted as Py-Na-FER, CHA-Na-FER, PI-Na-FER, En-Na-FER, and Pyrr-HF-FER) were synthesized using various SDAs in the different synthetic mediums. Rietveld refinements against PXRD data of as-made and Py-adsorbed samples reveal that Al atoms of **FER**-type zeolites were constrained at T1 and/or T3 sites. BASs associated with two both sites are inactive centers for the DME carbonylation reaction. Therefore, **FER**-type zeolites showed a lower synthesis rate of MA compared with **MOR**-type zeolite. And this is the reason why the improvement of MA synthesis rate is limited through changing OSDAs, synthetic methodologies, and synthetic mediums. Our unprecedented findings and characterization methodologies presented here will shed lights on the investigations of structure-activity relationships in the zeolite-related research fields.

Supporting Information

Supporting information is available in the online version of this article.

References

- [1] P. Tian, Y. Wei, M. Ye, Z. Liu, ACS Catal., 2015, 5, 1922–1938.
- [2] Q. Zhang, J. Yu, A. Corma, Adv. Mater., 2020, 32, 2002927.
- [3] H. Ham, H. S. Jung, H. S. Kim, J. Kim, S. J. Cho, W. B. Lee, M. J. Park, J. W. Bae, ACS Catal., 2020, 10, 5135–5146.
- [4] K. Cao, D. Fan, L. Li, B. Fan, L. Wang, D. Zhu, Q. Wang, P. Tian, Z. Liu, ACS Catal., 2020, 10, 3372–3380.

Graphical Abstract

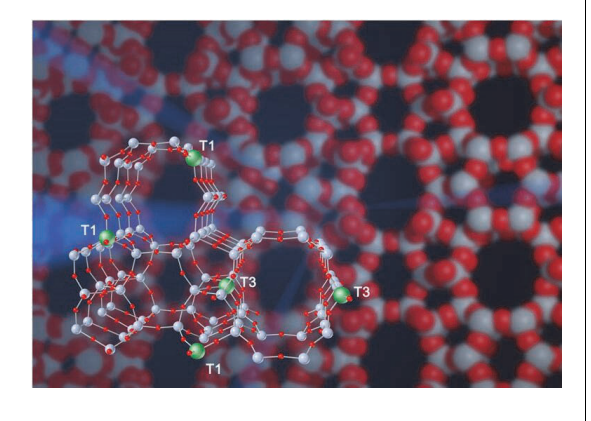
Chin. J. Catal., 2021, 42: 2078–2087 doi: 10.1016/S1872-2067(21)63884-6

Constrained Al sites in FER-type zeolites

Weifeng Chu, Xiaona Liu, Zhiqiang Yang, Hiroya Nakata, Xingzhi Tan, Xuebin Liu, Longya Xu, Peng Guo *, Xiujie Li *, Xiangxue Zhu * Dalian Institute of Chemical Physics, Chinese Academy of Sciences, China; BP (China) Dalian Office, China;

University of Chinese Academy of Sciences, China; Kyocera Corporation, Japan

Rietveld refinements against PXRD data reveal that Al atoms of **FER**-type zeolites are constrained at T1 and/or T3 sites no matter what types of structure-directing agents or synthetic medium are utilized. This finding well explains the low activity of **FER**-type zeolites catalyst in the dimethyl ether carbonylation reaction since Brönsted acid sites in the open channels, e.g., at T1 and T3 sites, cannot act as the active centers for this reaction.



- [5] J. Liu, H. Xue, X. Huang, P. Wu, S. Huang, S. Liu, W. Shen, Chin. J. Catal., 2010, 31, 729–738.
- [6] P. Cheung, A. Bhan, G. J. Sunley, E. Iglesia, Angew. Chem. Int. Ed., 2006, 45, 1617–1620.
- [7] F. E. Paulik, J. F. Roth, Chem. Commun., 1968, 1578–1578.
- [8] G. J. Sunley, D. J. Watson, Catal. Today, 2000, 58, 293–307.
- [9] A. Bhan, A. D. Allian, G. J. Sunley, D. J. Law, E. Iglesia, J. Am. Chem. Soc., 2007, 129, 4919–4924.
- [10] Y. Roman-Leshkov, M. Moliner, M. E. Davis, J. Phys. Chem. C, 2011, 115, 1096–1102.
- [11] A. B. Pinar, C. Marquez-Alvarez, M. Grande-Casas, J. Perez-Pariente, J. Catal., 2009, 263, 258–265.
- [12] J. Dedecek, M. J. Lucero, C. Li, F. Gao, P. Klein, M. Urbanova, Z. Tvaruzkova, P. Sazama, S. Sklenak, J. Phys. Chem. C, 2011, 115, 11056–11064.
- [13] S. Wang, L. Zhang, S. Li, Z. Qin, D. Shi, S. He, K. Yuan, P. Wang, T. Zhao, S. Fan, M. Dong, J. Li, W. Fan, J. Wang, J. Catal., 2019, 377, 81–97.
- [14] C. Marquez-Alvarez, A. B. Pinar, R. Garcia, M. Grande-Casas, J. Pérez-Pariente, *Top. Catal.*, 2009, 52, 1281–1291.
- [15] W. Chu, X. Li, S. Liu, X. Zhu, S. Xie, F. Chen, Y. Wang, W. Xin, L. Xu, J. Mater. Chem. A, 2018, 6, 12244–12249.
- [16] P. Feng, X. Chen, X. Li, D. Zhao, S. Xie, L. Xu, G. He, *Microporous Mesoporous Mater.*, 2017, 239, 354–362.
- [17] A. B. Pinar, L. Gomez-Hortigüela, L. B. McCusker, J. Perez-Pariente, Chem. Mater., 2013, 25, 3654–3661.
- [18] L. Wang, H. Xu, N. Yan, S. Correll, S. Xu, P. Guo, P. Tian, Z. Liu, CrystEngComm, 2018, 20, 699–702.
- [19] A. Martucci, A. Alberti, G. Cruciani, P. Radaelli, P. Ciambelli, M.

- Rapacciulo, Microporous Mesoporous Mater., 1999, 30, 95-101.
- [20] E. Artacho, E. Anglada, O. Dieguez, J. D. Gale, A. Garcia, J. Junquera, R. M. Martin, P. Ordejon, J. M. Pruneda, D. Sanchez-Portal, J. M. Soler, J. Phys.: Condens. Matter, 2008, 20, 064208.
- [21] M. Hammouri, S. K. Jha, I. Vasiliev, J. Phys. Chem. C, 2015, 119, 18719–18728.
- [22] N. Kaltsoyannis, J. E. McGrady, Principles and applications of density functional theory in inorganic chemistry II; Structure and bonding, Springer, Berlin, Heidelberg, 2004.
- [23] J. P. Perdew, K. Burke, M. Ernzerhof, Phys. Rev. Lett., 1996, 77, 3865–3868.
- [24] J. P. Perdew, K. Burke, M. Ernzerhof, Phys. Rev. Lett., 1997, 78, 1396–1396.
- [25] D. R. Hamann, M. Schluter, C. Chiang, Phys. Rev. Lett., 1979, 43, 1494–1497.
- [26] S. Grimme, J. Comput. Chem., 2006, 27, 1787-1799.
- [27] International Zeolite Association's Structure Commission http://www.iza-structure.org/index.htm.
- [28] D. E. Akporiaye, H. Fjellvag, E. N. Halvorsen, T. Haug, A. Karlsson, K. P. Lillerud. Chem. Commun., 1996, 1553–1554.
- [29] B. J. Campbell, A. K. Cheetham, G. Bellussi, L. Carluccio, G. Perego, R. Millini, D. E. Cox, Chem. Commun., 1998, 1725–1726.
- [30] X. Liu, Y. Cao, N. Yan, C. Ma, L. Cao, P. Guo, P. Tian, Z. Liu, Chin. J. Catal., 2020, 41, 1715–1722.
- [31] N. Yan, C. Ma, Y. Cao, X. Liu, L. Cao, P. Guo, P. Tian, Z. Liu, Small, 2020, 16, 2000902.
- [32] P. Feng, G. Zhang, X. Chen, K. Zang, X. Li, L. Xu, Appl. Catal. A, 2018, 557, 119–124.

FER分子筛中铝原子的受限落位

楚卫锋^{a,†}, 刘晓娜^{b,d,†}, 杨志强^c, Nakata Hiroya^e, 谭兴智^c, 刘雪斌^c, 徐龙伢^a, 郭 鹏^{b,\$}, 李秀杰^{a,#}, 朱向学^{a,*}

^a中国科学院大连化学物理研究所,催化基础国家重点实验室,辽宁大连116023,中国 ^b中国科学院大连化学物理研究所,洁净能源国家实验室,甲醇制烯烃国家工程实验室, 国家能源低碳催化与工程研发中心,辽宁大连116023,中国 ^c碧辟(中国)大连办公室,能源创新实验室,辽宁大连116023,中国 ^d中国科学院大学,北京100049,中国 [°]京瓷株式会社,先进材料与器件研究所,京都,日本

摘要: 分子筛是一类具有规则孔道或笼状结构的多孔材料, 因其独特的结构和可调的酸性而广泛用于石油化工、精细化学品合成、现代煤化工等诸多行业. 2006年Iglesia等在具有8元环孔道结构/侧口袋的FER和MOR分子筛上实现了无卤素添加、无贵金属存在条件下, 由二甲醚羰基化合成乙酸甲酯的反应. 乙酸甲酯通过进一步加氢可实现煤基乙醇的绿色生产. MOR分子筛通常具有较高的催化活性, 但失活迅速; FER分子筛表现出良好的催化稳定性, 但活性较低. 如何在保证FER分子筛稳定性的前提下, 进一步提升其羰基化活性是目前研究的热点. 前期理论和实验研究发现, 二甲醚羰基化反应活性与分子筛8元环孔道中的Brönsted酸位密度存在正相关. 因此, 通过优化合成条件, 选择性调控铝原子分布在"ferrierite"笼中, 可以提高FER分子筛的羰基化反应活性. 尽管研究者已在调节FER分子筛铝分布方面进行了大量研究, 但对于不同T位上Al原子的精准识别以及对应Brönsted酸位的可接触性还缺少系统和深入的认识.

本文选取了几种代表性模板剂,分别在碱性和含氟体系下制备了系列FER分子筛样品,利用Rietveld精修和模拟退火算法,在原子水平揭示了模板剂种类以及合成介质变化对AI原子在不同T位分布的影响,并结合二甲醚羰基化反应进行了结构和性能的关联.首先选取不同尺寸大小的环状胺(环己胺、哌啶、吡啶、吡咯烷)和链状胺(乙二胺)合成了具有相似形貌、孔结构、酸密度的系列FER分子筛样品.以CHA-Na-FER为例,PXRD精修结果显示,Na⁺(平衡35%的骨架负电荷)分布在10元环孔道中与O1形成氢键,质子化的环己胺分布在"ferrierite"笼中,并且环己胺上的N与O3形成氢键.这说明与O1相连的T3位以及与O3相连的T1位都有可能是AI富集的位置.为了进一步验证该结论,本文还精修了吸附探针分子吡啶的样品CHA-Na-FER-Py-60h.原粉以及吸附吡啶样品的精修结果表明,T1位和T3位是样品中铝富集的位置.随后,运用相同方

法研究了Py-Na-FER, PI-Na-FER, En-Na-FER和Pyrr-HF-FER样品中的AI落位,发现T1/T3位均是样品中AI富集的位置.此外,理论计算结果表明T1/T3位上AI原子的取代能较低,说明AI优先取代T1/T3位上的Si,这与精修结果相一致.

综上, 有机模板剂的选择与合成介质的改变对**FER**分子筛中Al分布的调控作用是有限的, 即Al原子总是优先分布于T1/T3位. 而与T1和T3位相关的Brönsted酸位不是二甲醚羰基化反应的活性位点. 因此与**MOR**相比, **FER**分子筛在二甲醚羰基化反应中表现出较低的催化活性.

关键词: FER分子筛; 铝落位; 结构表征; Brönsted酸位; 二甲醚羰基化

收稿日期: 2021-04-07. 接受日期: 2021-05-28. 上网时间: 2021-08-20.

- *通讯联系人. 电话/传真: (0411)84379279; 电子信箱: zhuxx@dicp.ac.cn
- [#]通讯联系人. 电话/传真: (0411)84379279; 电子信箱: xiujieli@dicp.ac.cn
- ^{\$}通讯联系人. 电话: (0411)84379149; 传真: (0411)84379289; 电子信箱: pguo@dicp.ac.cn

基金来源: 国家自然科学基金(21972136, 22008229, 21773233, 21991091, U20A20120); 中国科学院百人计划(Y706071202); 中国科学院洁净能源创新研究院合作基金(DNL201908); 兴辽英才计划(XLYC1908010, XLYC1901006); 碧辟能源创新实验室; STOE 李学全

本文的电子版全文由Elsevier出版社在ScienceDirect上出版(http://www.sciencedirect.com/journal/chinese-journal-of-catalysis).

[†]共同第一作者.